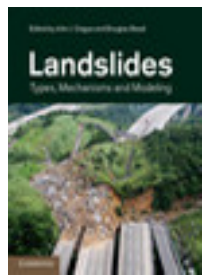


Landslides

Types, Mechanisms and Modeling

Edited by John J. Clague, Douglas Stead

Book DOI: http://dx.doi.org/10.1017/CBO9780511740367

Online ISBN: 9780511740367

Hardback ISBN: 9781107002067

Chapter

3 - Earthquake ground motion and patterns of seismically induced lands

liding pp. 24-36

Chapter DOI: http://dx.doi.org/10.1017/CBO9780511740367.004

Cambridge University Press

# 3 Earthquake ground motion and patterns of seismically induced landsliding

NIELS HOVIUS AND PATRICK MEUNIER

## ABSTRACT

Earthquake strong ground motion changes stresses in hillslopes and reduces the strength of surface materials. This can cause landsliding during earthquakes and enhance rates of slope failure in epicentral areas for longer periods. Rates of earthquake-triggered landsliding are strongly correlated with measured peak ground acceleration. Patterns of landslide density reflect the attenuation of seismic waves and geologic and topographic site effects. Using historic thrust fault ruptures with well-documented ground motion and landslide distributions as examples, we illustrate the links between earthquake mechanisms, seismic wave propagation, and triggered landsliding. The examples have shared geomorphic attributes: a maximum density of triggered landslides where earthquake slip is greatest; a progressive decrease of landslide density away from this maximum; clustering of triggered landslides on topographic ridges and other convex landscape elements; and preferential failure of slopes facing away from the earthquake source. We also show that rates of landsliding can remain high after an earthquake in a geomorphic crisis that fades over a period of years. Continued landsliding adds to the total erosion caused by an earthquake, reducing or possibly canceling seismic surface uplift. The examples underline the potential for the quantitative prediction of patterns of seismically triggered and induced landsliding, use of observed landslide patterns for study of earthquake mechanisms, and inclusion of seismically driven erosion in landscape evolution models.

## 3.1 INTRODUCTION

Intermediate and large shallow earthquakes can cause landsliding in steep terrain (Oldham, 1899; Mathur, 1953; Pain and Bowler, 1973; Wilson and Keefer, 1979; Harp and Jibson, 1996; Chigira *et al.*, 2010), mainly due to strong ground motion and the associated weakening of the hillslope substrate. Attenuation of seismic waves and topographic site effects give rise to distinct patterns of earthquake strong ground motion. These patterns are reflected in the density of earthquake-triggered landslides on a regional scale, but also within individual topographic features such as hills and mountain ridges. Their effect may persist over time and govern landslide patterns years after an earthquake. Erosion by later, seismically induced, landslides can add substantially to erosion during an earthquake, and affect the topographic change caused by that earthquake. Quantitative evaluations of the patterns of seismically triggered and induced landslides not only help explain the role of earthquakes in mountain building, but also reveal details of the earthquake mechanisms by which they were caused. Moreover, they offer insights into sediment production, landscape evolution, earthquake mechanisms, and seismic hazard risk management and mitigation, with considerable potential for further progress.

## 3.2 EARTHQUAKES, SEISMIC WAVES, AND GROUND MOTION

Earthquakes occur in solid Earth materials where sufficient elastic strain has accumulated to cause fault rupture. Progressive relative displacement of two geologic blocks separated by a potential or existing fault leads to increased stress and therefore stored strain energy in the rock mass around the fault zone. When the stress exceeds the rock mass strength, sudden failure can occur and stored energy is released. The released energy is used in fracture propagation, permanent displacement of mass, and associated frictional heating, and, importantly, is radiated in elastic strain seismic waves. These seismic waves travel through

*Landslides: Types, Mechanisms and Modeling*, ed. John J. Clague and Douglas Stead. Published by Cambridge University Press.

the Earth as body waves and along Earth's surface. Body waves radiate outward along curved raypaths that are affected by variations in rock density and stiffness, expanding geometrically until their energy has dissipated. The effect of seismic wave attenuation with distance ($R$) from source is described in its simple form by:

$$A_{(R)} \propto \frac{A_0}{R} e^{\frac{\pi . - f R}{v Q}} \tag{3.1}$$

where $A$ is the amplitude of the seismic wave, $f$ and $v$ are its frequency and velocity, respectively, the subscript 0 denotes the source, and $Q$ is a so-called "quality factor" representing energy dissipation due to anelasticity of the rock mass, scattering of waves on geologic structures, and other effects (Taylor *et al.*, 1986; Trifunac, 1994). Surface waves form where sufficient energy reaches the Earth's surface. These waves travel at lower velocities than body waves, but can have considerable amplitudes. The arrival of seismic waves can cause strong motion with directional or orbital shear (Bindi *et al.*, 2010). The combination of these phenomena constitutes an earthquake. Larger earthquakes release more stored energy than smaller ones, causing waves with larger initial amplitudes and attenuation distances. For a given frequency of incoming waves, the greater their amplitude, the larger the resultant ground velocities and accelerations.

The radiation pattern of seismic waves is determined by the focal mechanism of the earthquake (Sommerville *et al.*, 1997, 1999; Anderson *et al.*, 2000). In dip–slip events, motion is perpendicular to the strike of the fault plane. Such fault planes commonly have slopes <60°. In normal faults, the hanging wall moves down with respect to the footwall; and in reverse or thrust faults, it moves up. In both types of dip–slip events, most of the upward projected energy is released into the hanging wall, with significantly less strong ground motion in the footwall (Abrahamson and Somerville, 1996; Allen *et al.*, 1998; Shi *et al.*, 1998; Ogelsby *et al.*, 2000). Because rocks are stronger in compression than in tension, thrust fault earthquakes can be larger than normal fault earthquakes. Moreover, most topographic relief associated with thrust faults is located in the uplifting hanging wall. In contrast, topographic relief associated with normal faults is located in the footwall, the surface of the subsiding hanging wall being evened by deposition. The combination of these factors makes thrust fault earthquakes much more likely to cause significant and widespread landsliding than normal fault earthquakes. Most strike–slip faults are steep (>60°). Earthquakes on such faults commonly result in a more symmetric pattern of strong ground motion, with possible variations along the length of the structure due to directionality of the rupture propagation.

The energy released in an earthquake, expressed as the moment magnitude $M_w$, is equal to the rigidity of the rock mass multiplied by the product of slip on the fault and the size of the area that slipped. In small earthquakes ($M_w$ <6), relatively small amounts of slip (<1 m) are commonly distributed in a simple way over a slip patch of limited size (length $\leq 10^1$ km). This simple slip distribution makes it possible, for our purposes, to treat such earthquakes as point sources of energy. Larger earthquakes tend to have more extensive and often more complex rupture patterns (Wells and Coppersmith, 1994), with one or multiple slip patches moving along a fault or an array of faults as the earthquake develops. This gives rise to more complex patterns of energy release (Sommerville *et al.*, 1999). Therefore, large earthquakes are better treated as two-dimensional sources of energy, extending over distances of 100 km or more, with segmentation in the most complex cases. For example, the $M_w$ 7.6 Chi-Chi earthquake in central-west Taiwan in 1999 ruptured the north–south trending Chelungpu fault over a distance of about 110 km, with slip increasing from *ca*. 3 m in the south to more than 8 m in the north (Kao and Chen, 2000; Shin and Teng, 2001). Similarly, the $M_w$ 7.9 Wenchuan earthquake in Sichuan Province, China, in 2008, ruptured an array of faults over a distance of *ca*. 200 km, with displacements locally exceeding 10 m and different types of displacement on individual fault segments (Shen *et al.*, 2009). In such cases, treatment of the earthquake as a simple line source, or even a point source of energy, can lead to erroneous conclusions.

A further, relevant complication arises from the fact that, close to faults, peak ground accelerations have been found to saturate with increasing earthquake magnitude (Boore and Atkinson, 2008; Chiou and Youngs, 2008), possibly caused by the dynamics of the earthquake itself or by the geometry of large events (Anderson, 2000). Saturation implies that surface locations close to the rupture may be impervious to earthquake magnitude above a threshold, whereas locations farther afield experience ground motion in proportion to the magnitude of the earthquake. The length scale over which saturation occurs is likely to increase with earthquake size (Schmedes and Archuleta, 2008).

## 3.3 LANDSLIDING AND EARTHQUAKE STRONG GROUND MOTION

Similar to fault rupture, hillslope failure occurs when the shear stress across a potential failure plane exceeds substrate strength. The addition of earthquake strong ground motion to the ambient gravitational acceleration results in short-lived, cyclic changes of the normal and shear stresses in hillslopes during earthquakes (Newmark, 1965). Strong ground motions may lead to instantaneous failure due to initial or peak ground motion, or because of progressive substrate weakening due to rock mass fracturing (Harp and Jibson, 1996; Lin *et al.*, 2008; Meunier *et al.*, 2008) or breakage of the binding plant root mass over multiple ground motion cycles (Meisling and Sieh, 1980). The greater the amplitude of the incoming seismic waves and the duration of shaking, the greater the likelihood of failure of a steep slope, primed by other erosional processes such as fluvial incision (Kelsey, 1988; Burbank *et al.*, 1996; Densmore

and Hovius, 2000). It is therefore expected that relations exist between the magnitude of an earthquake and the extent and intensity of the landsliding it causes.

Global compilations of earthquake and landslide data have been used to explore the effect of earthquake magnitude on the extent of the area affected by landsliding. For example, Keefer (1984) and Rodriguez *et al.* (1999) have tentatively defined maximum affected areas for earthquakes of different magnitudes. Such analyses should take into account the depth and focal mechanism of earthquakes, the frequencies at which seismic waves carry most energy, and the local geology and topography. Source depth is of crucial importance (implicit in the term $R$ in Eq. 3.1), especially in intermediate-sized earthquakes in which the amplitude of seismic waves is likely to attenuate within tens of kilometers to values that do not cause notable landsliding. Therefore, the inclusion of earthquakes with focal depths as large as *ca*. 70 km (Keefer, 1984; Rodriguez *et al.*, 1999) is bound to cause departures from any trend set by shallow events (depth <20 km). Moreover, as low-frequency waves travel farther than high-frequency ones, the dominant frequency of seismic waves ($f$ in Eq. 3.1), which can differ between earthquakes, affects the relevant attenuation length, as do geologic factors ($Q$ in Eq. 3.1). Analyses of global relationships between earthquake moment magnitude and landslide number or concentration (Keefer, 2002), area density, and even volume (Malamud *et al.*, 2004) should therefore be approached with caution.

It is, then, perhaps most productive to consider patterns of landsliding in terms of a geophysical quantity that directly affects slope stability: strong ground motion or, more specifically, ground velocity or acceleration (Luzi and Pergalani, 2000). For many intermediate and large earthquakes that have caused substantial landsliding, insufficient instrumental data exist to evaluate the relation between peak ground velocity (PGV) or peak ground acceleration (PGA) and landsliding. However, where data exist, a strong correlation of ground motion and landslide density (percent area affected by landsliding, $A_{ls}$) has been found. This relation appears to take a linear form (Meunier *et al.*, 2007):

$$A_{ls} = \alpha \mathrm{PGA} - \beta \tag{3.2}$$

where $\alpha$ is a susceptibility coefficient and $\beta = \alpha \mathrm{PGA}_{cr}$, the minimum ground acceleration required to trigger substantial slope failure (Fig. 3.1). These empirically constrained constants have location-specific values. For >20,000 landslides triggered by the 1999 Chi-Chi earthquake, $\alpha = 2.7\ g^{-1}$ ($5.8\ g^{-1}$) and $\beta = 0.5$ (0.6), where $g$ is the gravitational acceleration, with a regression coefficient $|R| = 0.75$ (0.87) for the horizontal component of PGA (values for the vertical component in parentheses), measured at seven stations in the epicentral area (Dadson *et al.*, 2004). For >11,000 landslides caused by the $M_w$ 6.7 Northridge, California, earthquake in 1994 (Harp and Jibson, 1996), $\alpha = 15.5\ g^{-1}$ ($15.4\ g^{-1}$) and $\beta = 3.3$ (1.4), with $|R| = 0.96$ (0.97). And for >10,000 landslides triggered by the 2004 Chuetsu, Niigata earthquake in Japan (Osanai *et al.*, 2007), $\alpha = 2.4\ g^{-1}$ ($2.6\ g^{-1}$) and $\beta = 1.5$ (0.7), with $|R| = 0.64$ (0.89). In all cases, best-fit regressions have a horizontal acceleration threshold of $\mathrm{PGA}_{cr} \approx 2\ \mathrm{m\,s^{-2}}$, below which no landslides occurred, despite contrasting climate, relief, and substrate lithology. This threshold applies to failure of the weakest material, regolith, and soil on slopes, the frictional strength of which is relatively uniform over large areas.

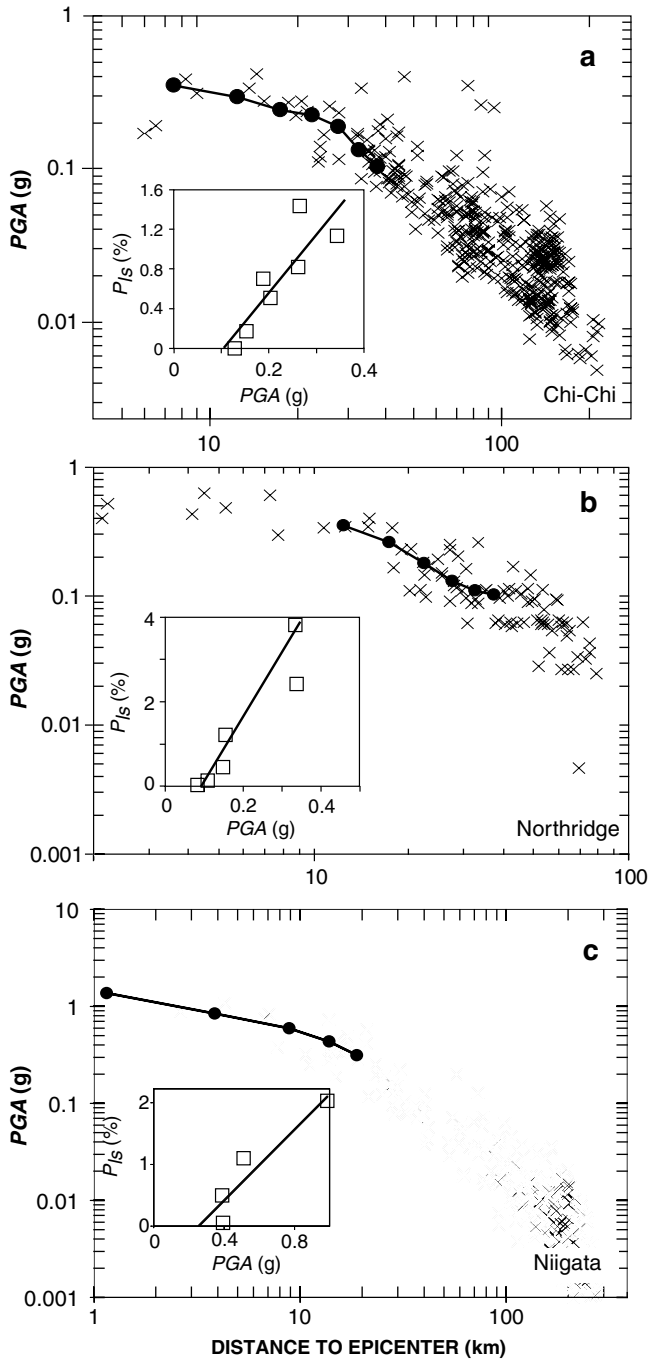


**Fig. 3.1.** Average landslide density plotted against average vertical PGA for 5-km windows parallel to the fault trend with least squares linear regressions for (a) the 1999 Chi-Chi earthquake (PGA data from Central Weather Bureau, Taipei, Taiwan), (b) the 1994 Northridge earthquake (PGA data from Trifunac and Todorovska, 1996), and (c) the 2004 Niigata earthquake (Honda *et al.*, 2005). (After Meunier *et al.*, 2007; result for the 2004 Niigata earthquake has not been published elsewhere.)

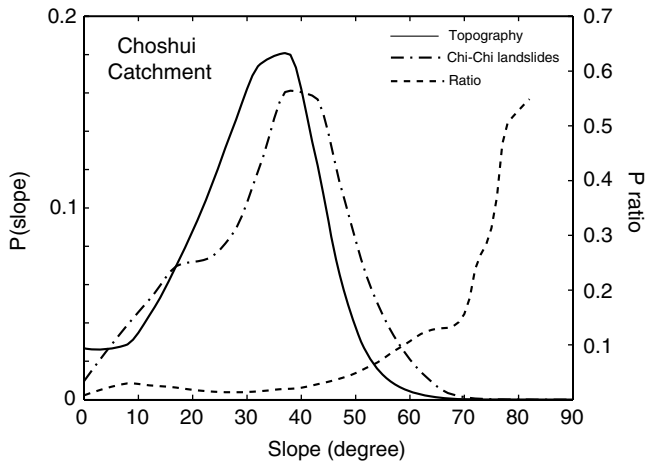


**Fig. 3.2.** Probability distribution of all topographic slopes (solid line) and slopes affected by earthquake-triggered landsliding (dashed/dotted line; >20,000 landslides) in the Choshui catchment, draining the epicentral area of the 1999 Chi-Chi earthquake. Local topographic slopes have been calculated as the steepest slope within a square of 3 × 3 DEM grid cells. The dashed line is the ratio of the probabilities of all slopes and failed slopes for a given gradient; it is an objective measure of the failure susceptibility. The steepest slopes were most prone to failure during the Chi-Chi earthquake.

Within epicentral areas, rock types can have distinct and different landslide susceptibilities that overprint large-scale patterns of earthquake-triggered landsliding. This effect was shown by Parise and Jibson (2000) for the Northridge earthquake and strongly influenced landslide density patterns of the 2008 Wenchuan earthquake (Yin *et al.*, 2010; Dai *et al.*, 2011) and several recent intermediate-sized earthquakes in Japan (Wang *et al.*, 2007; Kawabata and Bandidas, 2009; Yagi *et al.*, 2009). Moreover, landslide susceptibility is also affected by topography. Topographic gradient is a primary control on slope stability; it partitions gravitational pull into a slope-normal, motion-arresting component and a slope-parallel, shear-inducing component. The result is an increasing likelihood of failure with increasing topographic gradient for a given substrate. This relation can be shown by comparing the probability distribution of local slope values on a given length scale in a landscape and the equivalent probability distribution of failed slopes in that landscape (Fig. 3.2; Lin *et al.*, 2008). The latter normalized by the former is an objective, albeit general, index of the susceptibility of topographic slopes to failure. A landscape with a higher average slope susceptibility index is likely to sustain more landsliding during a given earthquake.

Despite sparse empirical evidence, and mindful of the geologic and topographic controls on landslide susceptibility, we propose that the correlation of peak ground acceleration and landslide density is strong and real and that it is the key to understanding the global attributes of regional and local patterns of earthquake-induced landsliding. Landslide patterns also provide insights into mechanisms of faulting. Further tests of the applicability of Eq. 3.2, and improved understanding of controls on the landslide susceptibility coefficient $a$ and threshold constant $\beta$, will depend on studies of future earthquakes in well-instrumented areas and retrospective analysis of well-documented historic cases, and should be considered a priority for research.

## 3.4 SPATIAL PATTERNS OF EARTHQUAKE-TRIGGERED LANDSLIDES

### 3.4.1 REGIONAL PATTERNS

Attenuation of seismic waves with increasing distance from the source (Eq. 3.1) and the relation between peak ground acceleration or velocity and landslide rate (Eq. 3.2) give rise to clear patterns of landslide density within an area affected by earthquake strong ground motion. Meunier *et al.* (2007) calculated landslide density, $P_{ls}$, as the percentage of area with topographic slope >20 percent (an arbitrary threshold) affected by earthquake-triggered landsliding. They plotted $P_{ls}$ against distance from the projected surface trace of the seismogenic fault for three large thrust earthquakes with shallow (<20 km) hypocenters: the 1999 Chi-Chi earthquake; the 1994 Northridge earthquake; and a pair of $M_w$ 6.9 and 6.7 earthquakes on the Ramu-Markham fault in northeast Papua New Guinea; the earthquakes were treated as linear sources of energy (Fig. 3.3). In all three cases, the landslide density peaked in the hanging wall of the seismogenic fault. Moreover, in the case of the 1999 Chi-Chi earthquake and also for the events on the Ramu-Markham fault, maximum landslide densities coincided with the earthquake epicenter. Away from the landslide density maximum, and farther into the hanging wall, $P_{ls}$ decreased quasi-exponentially, mirroring the geometric spreading and attenuation of seismic waves, while $P_{ls}$ dropped more steeply toward the surface trace of the faults. Other researchers have found similar patterns for the concentration of landslides (number per unit area) caused by the 1989 $M_w$ 6.9 Loma Prieta, California, earthquake (Keefer, 2002), and the 2004 $M_w$ 6.6 Chuetsu, Niigata, earthquake (Wang *et al.*, 2007). The Niigata earthquake had a large reverse dip–slip component of movement, like the Chi-Chi and Northridge events (Spudich, 1996; Shin and Teng, 2001), and its landslide pattern shares all the essential characteristics of the other examples in Figure 3.3.

In the case of the 1994 Northridge earthquake, however, the landslide density peak was 8 km north of the epicenter, in the Santa Susanna Mountains. Steep topography is limited near the epicenter, but the landslide density distribution appears to reflect the pattern of energy release during the earthquake. The epicenter of the Northridge earthquake was located above the lower edge of the rupture plane in the flat San Fernando Valley. During the earthquake, as the rupture propagated upward and to the north along the fault plane, recorded ground accelerations remained high and approximately constant up to 10 km north of the epicenter (Todorovska and Trifunac, 1997), which may have set the landslide density pattern. Geomorphically

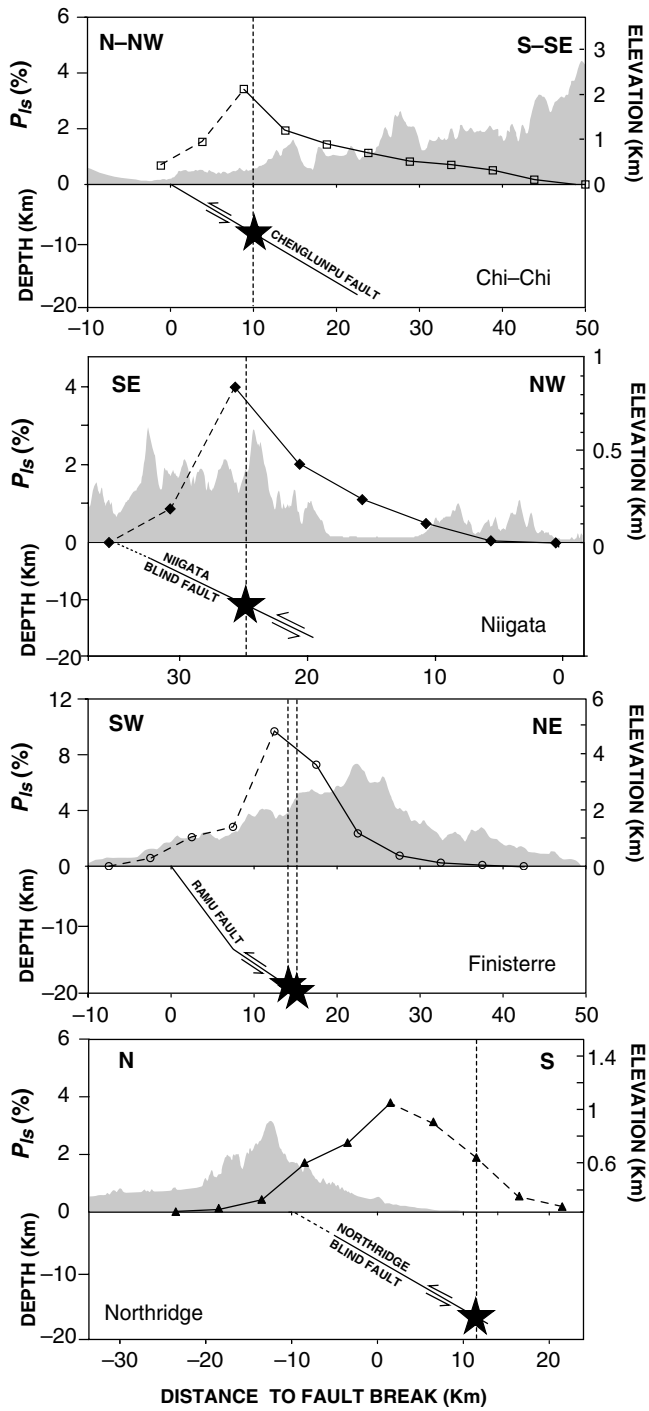


**Fig. 3.3.** Landslide density (percentage of total area) plotted against distance to the (projected) surface break of the seismogenic fault for the 1999 Chi-Chi, 2004 Niigata, 1993 Finisterre, and 1994 Northridge earthquakes. Fault planes are shown schematically; also shown are positions of earthquake hypocenters (stars). For the Chi-Chi, Finisterre, and Niigata earthquakes, the landslide density peak is located directly above the earthquake hypocenter; for the Northridge earthquake, the landslide density peak is 8 km north of the epicenter at the edge of the Santa Susanna Mountains. Topographic profiles across the epicenter, perpendicular to the fault, are shown in gray. (After Meunier *et al.*, 2007; result for the 2004 Niigata earthquake has not been published elsewhere.)

important energy release in large earthquakes can occur far from the earthquake hypocenter. Ideally, it is this pattern of energy release (Hikima and Koketsu, 2005; Suzuki *et al.*, 2010) that should be considered when analyzing earthquake-triggered landsliding, rather than the location of the epicenter. In many earthquakes, however, maximum peak ground motion is at the epicenter or at epicentral distance from the fault surface trace. Landslide density patterns with respect to fault traces observed elsewhere (Pearce and O'Loughlin, 1985; Owen *et al.*, 2008; Yagi *et al.*, 2009) might be better understood in this light.

Taking this approach one step further, we envisage that, based on Eq. 3.2, landslide density maps, weighted for the influence of topographic and geologic landslide susceptibility, can be perused for information about earthquake strong ground motion, and even inverted for constraints on the distribution of coseismic slip on a fault plane. If robust, this application could complement instrumental records of ground motion that are normally used for this purpose and, where such records are absent, open up a large number of poorly instrumented historic and future earthquakes for further seismological investigation.

### 3.4.2 TOPOGRAPHIC SITE EFFECTS

Local geologic and topographic features can have important effects on earthquake ground motion. For example, sediment fills of basins or valleys can significantly amplify earthquake ground motion relative to bedrock (Aki, 1993). Such amplification is attributed to the fact that sediments and weak rocks have a lower elastic modulus than strong rocks. Weak geologic materials will undergo a greater displacement for a given force exerted by an incoming seismic wave, although the effect may be nonlinear and may be reduced for large earthquakes (Field *et al.*, 1994). Where hillslopes are formed in weak materials, rates of earthquake-triggered landsliding can be disproportionately high, as was observed in the conglomerate badlands of the 99 Peaks area near the epicenter of the 1999 Chi-Chi earthquake (Hung, 2000). However, on many hillslopes, strong bedrock has only a thin and discontinuous sediment cover. Although this thin cover may locally amplify ground motion (Del Gaudio and Wasowski, 2007), other topographic site effects dominate local landslide patterns in steep uplands.

Large peak vertical accelerations have been recorded at ridge crests during several earthquakes. For example, during the 1987 $M_w$ 5.9 Whittier Narrows, California, earthquake, the amplitude of seismic waves recorded at the crest of 60-m-high Tarzana Hill was 10 times greater than that observed on the surrounding plains (Spudich *et al.*, 1996). On the same hill, instruments recorded a peak horizontal acceleration 1.78 times the gravitational acceleration during the 1994 $M_w$ 6.7 Northridge earthquake (Bouchon and Baker, 1996). Topographic amplification of ground accelerations occurs when seismic waves entering the base of a topographic ridge are partially reflected back into the rock mass and diffracted along the free surface. The seismic waves are progressively focused upward, and the constructive interference of their reflections and the associated diffractions

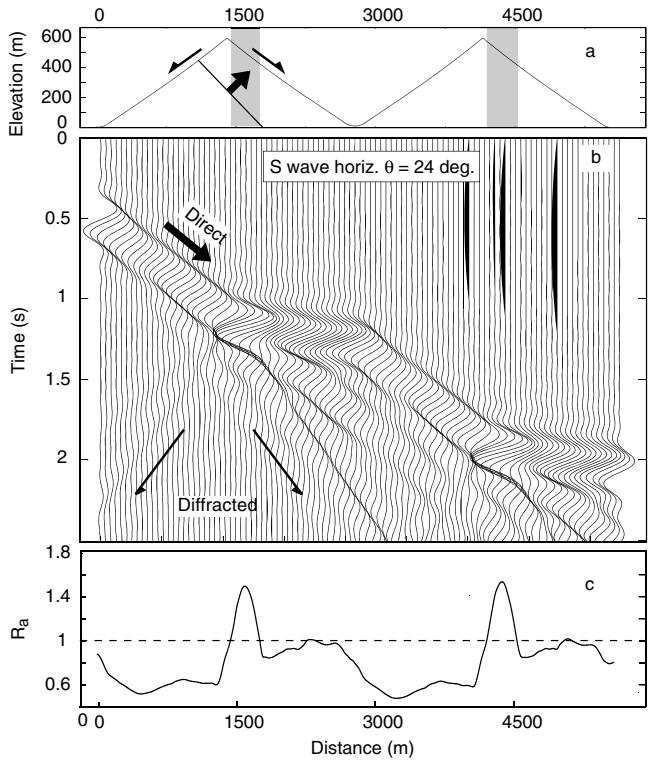


**Fig. 3.4.** Illustration of topographic site effects in a ridge-and-valley landscape. (a) Topographic profile consisting of two adjacent mountain ridges representing the average cross-profile of ridges in the Finisterre Mountains, Papua New Guinea. Ridge flanks are slightly concave-up and have a length of 1.6 km. (b) Synthetic accelerogram (ground acceleration recorded along the surface with time), generated along the topographic profile. The accelerogram is for the horizontal component of an S wave delta pulse (0–6 Hz) arriving from the left at an angle of 24° from the vertical. (c) Associated ratio, Ra, of local PGA in this model and local PGA in a flat-Earth equivalent. The direct wave interferes constructively with the diffracted wave generated at the ridge crest, causing amplification of the PGA on the ridge flank facing away from the wave source (gray zone in a). (From Meunier *et al*., 2008.)

increases toward the ridge crest, giving rise to enhanced ground accelerations on topographic highs (Fig. 3.4; Bouchon, 1973; Geli *et al*., 1988; Meunier *et al*., 2008). Topographic amplification values are typically small compared with those of sediment fills, but can be >2. Their effect is strongest on S waves, and the exact location of amplification maxima depends on the angle of wave incidence. Seismic waves with wavelengths greater than the base width of a ridge are unaffected by the topography (Meunier *et al*., 2008). As most of the energy of an earthquake is carried by waves with a relatively low frequency (<1 Hz), larger topographic features tend to be more prone to this effect than smaller features. Oblique incidence of seismic waves causes amplification maxima to shift away from ridge crests or hilltops and into slopes facing away from the earthquake epicenter. Secondary amplification maxima are predicted at smaller, convex-up knickpoints within ridge flanks. Elsewhere in ridge-and-valley landscapes, topographic site effects tend to cause de-amplification of ground motion with respect to the values expected for a "flat-Earth" equivalent.

Topographic site effects can be large enough to significantly affect slope failure during an earthquake (Havenith *et al*., 2003) and have been shown to govern patterns of landsliding in several large earthquakes (Meunier *et al*., 2008). Perhaps the clearest example is the 1994 Northridge earthquake, where 56 percent of the area affected by seismically triggered landslides was in the uppermost 25 percent of hillslopes (Fig. 3.5). We have found similar, but somewhat less pronounced, clustering of landslides triggered by the 1993 Ramu-Markham and the 2004 Niigata earthquakes (Fig. 3.5) and the 1999 Chi-Chi earthquake (Meunier *et al*., 2008). Moreover, secondary landslide clusters occurred near prominent knickpoints above inner gorges along the main valleys of the Finisterre Mountains, in the hanging wall of the Ramu-Markham fault. There, and in the area affected by the Chi-Chi earthquake, landslide rates were highest in slopes facing away from the earthquake epicenter, but – for poorly understood reasons – this effect was not found for the Northridge earthquake (Fig. 3.6).

Due in part to topographic site effects, most earthquake-triggered landslides do not connect directly with river channels and instead deposit debris on hillslopes and in debris-flow channels. As an example, in the Chenyoulan River catchment, south of the epicenter of the Chi-Chi earthquake, 88 percent of earthquake-induced landslides did not reach river channels (Lin *et al*., 2008). If landslides that did reach channels had the same size distribution as those that did not, then only one-tenth of mobile landslide debris was delivered direct to streams in the catchment. Much of the debris produced by an earthquake may initially remain in a landscape and become entrained in a prolonged downslope cascade of sediment involving multiple episodes of remobilization by mass wasting processes (Dadson *et al*., 2004). This effect introduces a time dimension to earthquake-induced erosion that will be explored further in the following sections.

## 3.5 TEMPORAL PATTERNS OF SEISMICALLY INDUCED LANDSLIDING

Substrate weakening through crack propagation and coalescence, and shear damage to vegetation root mass due to rapid cyclic stressing should result in a long-lived increase in slope failures in earthquake-affected areas. These effects are likely to be enhanced by the presence of new landslide debris and colluvium on hillslopes after an earthquake and by the occurrence of earthquake aftershocks. Progressive decay of the seismic moment of aftershocks, closure of cracks due to settling of the shaken rock mass, re-establishment of plant root networks, and erosional removal of debris and weakened materials will act over time to reduce rates of landsliding to background values. These restorative processes are likely to have different time constants, so that their combined effect is not necessarily a simple decay of the landslide rate after an earthquake. However, it is clear that in terms of mass wasting, an earthquake can be the start of a prolonged geomorphic crisis.

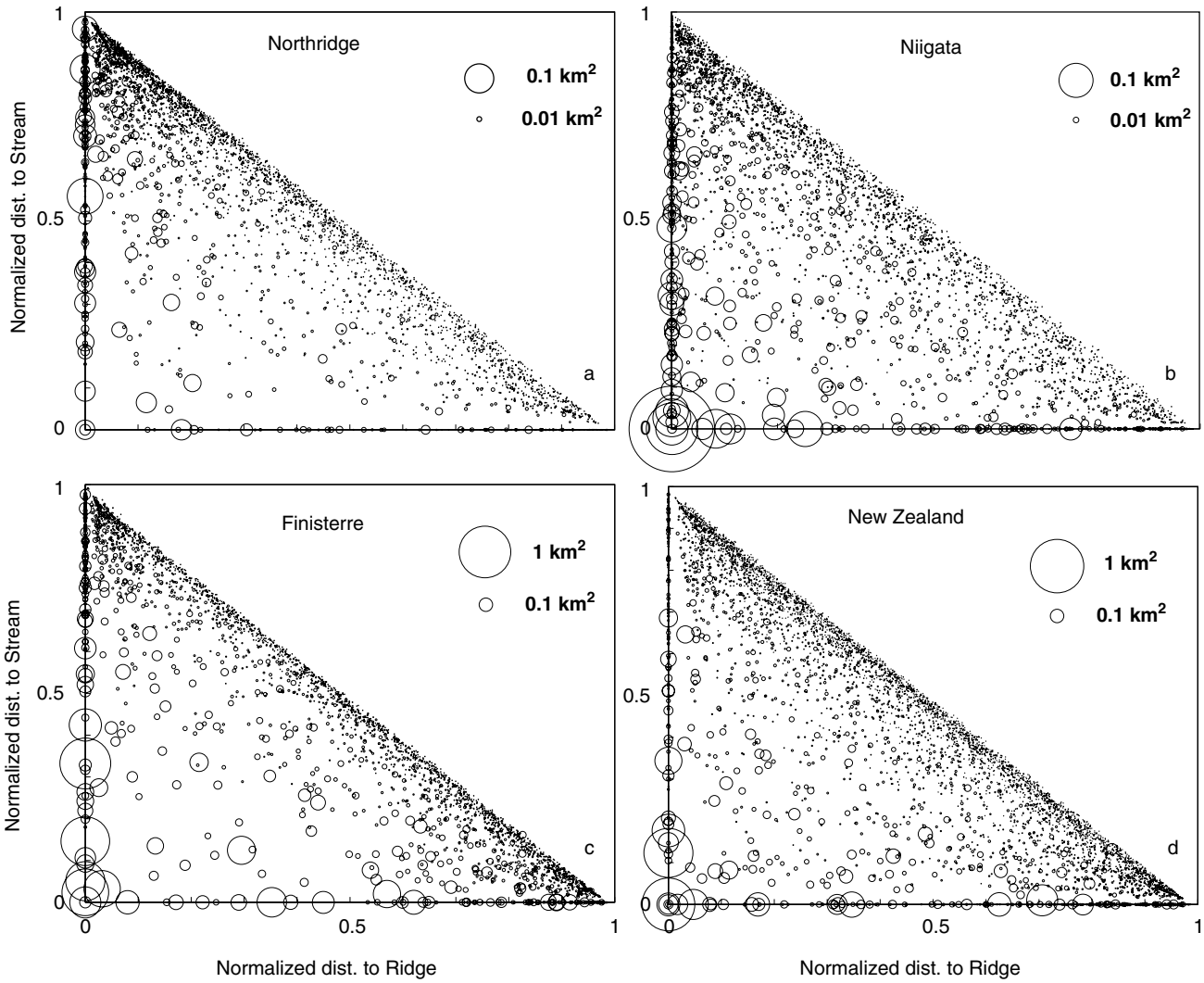


**Fig. 3.5.** Location of landslides with respect to a ridge crest and stream. Distances from the landslide crown to the nearest ridge and from the lowest point on the landslide lobe to the nearest stream have been measured along the line of steepest descent and normalized for the total length of the slope on which the landslide is located. The surface area of the landslide is indicated with a circle of variable diameter. Landslides triggered by (a) the 1994 Northridge earthquake and (b) the 2004 Niigata earthquake cluster around ridge crests. Landslides triggered by the 1993 earthquakes in the Finisterre Mountains (c) cluster at ridge crests and near the base of slopes. Rainfall-induced landslides in the western Southern Alps, New Zealand (d) are uniformly distributed. (After Meunier *et al*., 2008; result for the 2004 Niigata earthquake has not been published elsewhere.)

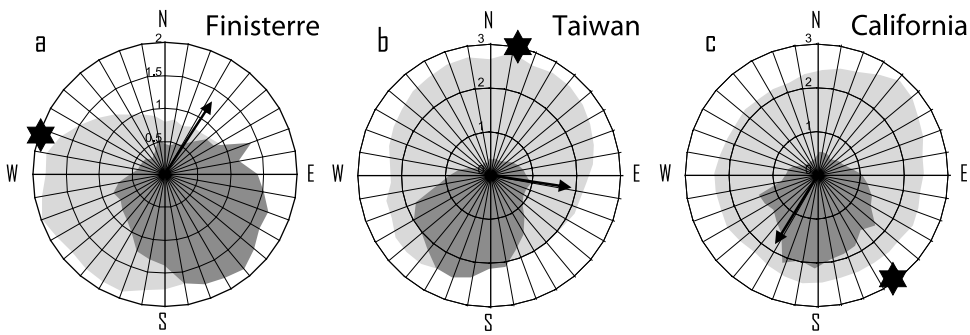


**Fig. 3.6.** Distribution of slope orientation (in percent; light gray) and normalized distribution of orientation of earthquake-triggered landslides (dark gray) in (a) the Finisterre Mountains, (b) central-west Taiwan, and (c) southern California. Arrows indicate the dip direction of the seismogenic fault. Stars indicate the relative mean position of the earthquake epicenter with respect to the landslides represented in these plots. (From Meunier *et al*., 2008.)

Studies of the temporal evolution of landsliding in a mountain catchment close to the epicenter of the 1999 Chi-Chi earthquake have confirmed the existence of a progressively decaying seismic perturbation of landslide rates (Lin *et al*., 2008; Hovius *et al*., 2011). In the Chenyoulan River catchment (*ca*. 400 km$^2$), directly south of the earthquake epicenter, the history of mass wasting is known from 16 landslide maps covering the period 1996–2006. A total of 8123 mapped landslides with a combined surface area of 31.5 km$^2$ occurred prior to the Chi-Chi earthquake, due mainly to typhoon rainfall. About 3800 mapped landslides with a combined area of 16 km$^2$ were attributed to the earthquake, and a remarkable 48,370 landslides with a total area of 221 km$^2$ occurred after the earthquake, up to the end of 2006. The post-earthquake landslides, many of which partially occurred at older landslide sites, were triggered by intense, but unexceptional typhoon rainfall. Their rate of occurrence strongly suggests that they were the indirect result of the Chi-Chi earthquake. Prior to 1999, landslides primarily occurred on slope segments adjacent to river channels. Rates of landsliding increased throughout the landscape due to the earthquake (Fig. 3.7), with maximum changes of up to 800 percent at a distance of 300–700 m from streams, and also 1700–2200 m from streams – where many of the principal ridges are located. Due to their convexity, these particular locations in the landscape were predisposed to the largest topographic site effects, confirming that the majority of landslides in this time window were earthquake-induced. Landslide rates have decayed steadily from a maximum in 2001, when the Chenyoulan catchment was first hit by a large typhoon after the earthquake. Moreover, landsliding has migrated to lower positions on hillslopes over this interval. In 2006, landslide rates on lower slopes had returned to pre-earthquake values, but they have remained somewhat elevated on higher slopes (Fig. 3.7b; Hovius *et al*., 2011).

It is unclear which processes played a role in the progressive restoration of pre-earthquake landslide conditions in the mountain landscape affected by the Chi-Chi earthquake and what determined the rate of this restoration. Restoration was largely unrelated to aftershocks, whose summed moment normalized within 15 months after the Chi-Chi earthquake, when landslide rates were still elevated (Hsu *et al*., 2009). Moreover, large decreases in groundwater level and pore water pressure were recorded in the epicentral area after the earthquake (Wang *et al*., 2001), but neither their duration (up to several months) nor the direction of these changes seem to be related to landsliding. Repair of tree root mass can take years or decades after an earthquake (Jacoby, 1997), similar to the timescale of the observed decrease of landslide rate. Finally, the evolution of landslide rates in the Chenyoulan catchment may have been a largely erosional phenomenon, without significant forcing by other factors. Nevertheless, its consequence was that the total amount of erosion due to the Chi-Chi earthquake was much greater than the erosion due to coseismic landsliding alone. It is likely that other large earthquakes have a similar prolonged legacy in landsliding, but quantitative assessments are rare (Koi *et al*., 2008), in spite of the implications for natural hazard risk, sediment fluxes, and the mass balance of earthquakes.

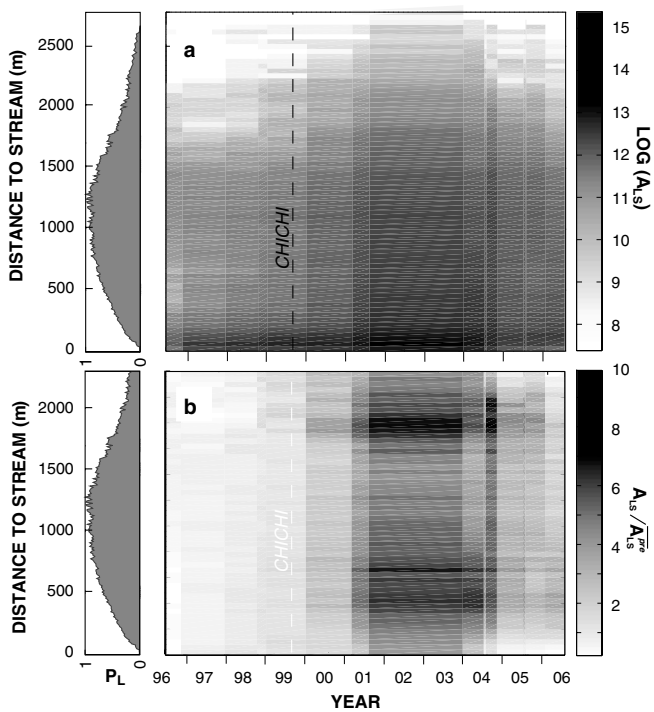


**Fig. 3.7.** Topographic location and intensity of landsliding in the Chenyoulan catchment, south of the epicenter of the 1999 Chi-Chi earthquake. (a) Time evolution of the area of landsliding, $A_{LS}$ (m$^2$), reported with flow distance to stream for the period 1996–2006. The stream network is the ensemble of locations with upslope area >1 km$^2$, a cut-off determined from slope-area scaling. Fifteen time intervals are delimited by landslide maps; the difference between successive maps represents landsliding within the interval. (b) Time evolution of the actual area of landsliding normalized by the area of landsliding prior to the Chi-Chi earthquake (dimensionless), reported with flow distance to stream. (Adapted from Hovius *et al*., 2011.)

## 3.6 EARTHQUAKE EROSION AND MASS BALANCE

Slip on faults creates topographic relief. Surface deformation along the fault trace is greatest where dip–slip faults break the Earth's surface (Avouac, 2007). On such faults, uplift and subsidence decrease with distance away from the fault trace in a pattern set by the geometry of the fault plane and the flexural rigidity of the geologic substrate. Pure strike–slip faults do not have much associated topography, other than on fault bends. Most faults have a combination of dip–slip and strike–slip displacement. Deeper earthquakes, for example at subduction zones, do not commonly build local relief, but instead affect surface elevation in a regionally distributed fashion. Finally, below the seismogenic zone, where temperatures and pressures are too high to permit the build-up of elastic strain and brittle failure, deformation is more gradual and is not associated with sudden displacements. Increasingly, it is recognized that gradual deformation, not involving macro-scale seismicity, may

also play an important role within the seismogenic zone (Liu and Rubin, 2010), but in many areas with high rates of crustal deformation, shallow earthquakes contribute significantly to the displacement of rocks and the surface (Avouac, 2007). The largest earthquakes dominate the cumulative seismic-moment release in mechanical work (Hanks and Kanamori, 1979), both globally (Bufe and Perkins, 2005) and on individual faults. Thus it is reasonable to expect that in seismically active areas, topographic relief is formed mainly by large earthquakes. However, as we have seen, in uplands with sufficiently steep relief, large earthquakes also cause slope failure and the conversion of rock mass into transportable sediment. Keefer (1994) and Malamud *et al*., 2004) have proposed a relationship between earthquake moment and landslide volume, attributing a larger erosional impact to larger earthquakes. If the products of seismically induced mass wasting are removed from the epicentral landscape (Pain and Bowler, 1973; Pearce and Watson, 1986, Dadson *et al*., 2004; Koi *et al*., 2008), erosion should be considered as a term in the mass balance of an earthquake.

The potential importance of induced erosion in the mass balance of an earthquake is underlined by the estimated 47 $km^3$ volume of landslides triggered by the 1950 Assam earthquake (M8.6) in the Tibet Himalayas (Mathur, 1953), and the 74–400 mm estimated average surface lowering by landslides caused by a M7.9 earthquake in the Torricelli Mountains of Papua New Guinea in 1935 (Simonett, 1967). These estimates were calculated without detailed constraints on landslide area–volume scaling (Keefer, 1999), and can therefore only serve as general indicators. Guzzetti *et al*. (2009) have shown that, globally, landslide area ($A$) and volume ($V$) are related by a power law, $V \propto A^{3/2}$. This relation makes it possible to derive first-order estimates of volumes of material mobilized by populations of landslides induced by an earthquake from comprehensive landslide polygon maps or area–frequency relations (Hovius *et al*., 1997). Such volume estimates can be paired with constraints on surface displacements associated with earthquakes. However, landslide volumes may differ by as much as two orders of magnitude for a given landslide area (Guzzetti *et al*., 2009). Moreover, population volume estimates based on landslide area–frequency relations are extremely sensitive to the exact value of the volume–area scaling exponent (Larsen *et al*., 2010). Thus, detailed knowledge of local conditions is required to reliably use this approach.

Parker *et al.* (2011) examined the potential changes in orogen volume resulting from the $M_w$ 7.9 2008 Wenchuan earthquake in Sichuan, China. The earthquake triggered more than 56,000 landslides, producing an estimated 5–15 $km^3$ of debris. This amount exceeds the net volume of 2.6 ± 1.2 $km^3$ added to the orogen by coseismic rock uplift (de Michele *et al*., 2010), implying that, even if only a fraction of landslide debris is removed from the orogen over the likely 2000–4000-year earthquake return period (Shen *et al.*, 2009), the Wenchuan earthquake will have caused a net material deficit in the Longmen Shan (Fig. 3.8). Similarly, Yanites *et al.* (2010) have estimated that 2–5 $km^3$ of debris was generated by earthquake-triggered landsliding within the 0.2 *g* contour of the 1999 Chi-Chi earthquake in Taiwan. Complete removal of the landslide material, according to these estimates, would give an average landscape lowering of 0.6–1.7 m (Yanites *et al.*, 2010), far exceeding the average surface uplift induced by the earthquake (Loevenbruck *et al*., 2004; Yu *et al*., 2001).

Observing that most landslides do not transfer mass over distances $>10^0$ km, Hovius *et al*. (2011) argued that it is geophysically more meaningful to consider the export of sediment from an earthquake-affected area, rather than the mass wasting within it. For the Chi-Chi earthquake, they demonstrated that river-suspended sediment concentrations peaked and relaxed in correspondence with landslide rates over a period of *ca*. 7 years. Knowing the expected values of sediment concentrations over the full range of river discharges for aseismic conditions, and assuming a constant proportionality of suspended load and bedload transport, they isolated the seismically induced component of sediment export from the epicentral area of the earthquake. They then distributed this erosion over the earthquake-affected area according to the pattern of earthquake-induced landslide density, subtracting from the co- and post-seismic surface deformation to obtain a conservative estimate of the net topographic effect of the Chi-Chi earthquake (Fig. 3.9). According to their estimates, sediment export removed >30 percent of the added rock mass from the epicentral area, resulting in a reduction of surface uplift by up to 0.25 m, or 35 percent of the local elevation change and a reduction of the area where the Chi-Chi earthquake had built topography. Moreover, they argued that even the largest local surface uplift due to the earthquake could be fully eroded within the earthquake return period.

Both the timescale and the efficiency of removal of earthquake-generated sediment from an epicentral area are likely to differ considerably between cases due to differences in hillslope-channel connectivity, the balance of fluvial transport capacity and sediment supply, and ponding behind landslide dams (Pain and Bowler, 1973; Pearce and Watson, 1986; Korup, 2005; Koi *et al*., 2008; Yanites *et al*., 2010). Nevertheless, it is clear that where crustal shortening is accommodated on a shallow detachment, mainly by slip in large earthquakes, average surface elevation is significantly reduced by erosion caused by the same mechanism that constructs topography. Seismically induced landsliding subdues the surface taper of frontal ranges and could hamper the recognition of active, seismogenic faults. This effect may be most pronounced on faults with a significant strike–slip component and reduced surface deformation.

## 3.7 CONCLUSIONS AND OUTLOOK

The association of landsliding and earthquake strong ground motion is universal in steep uplands. It gives rise to characteristic, and perhaps predictable, patterns of erosion during large earthquakes, the amplitude and geometry of which depend not only on the earthquake mechanism and location, but also on the attenuation and interference of seismic waves due to distance,

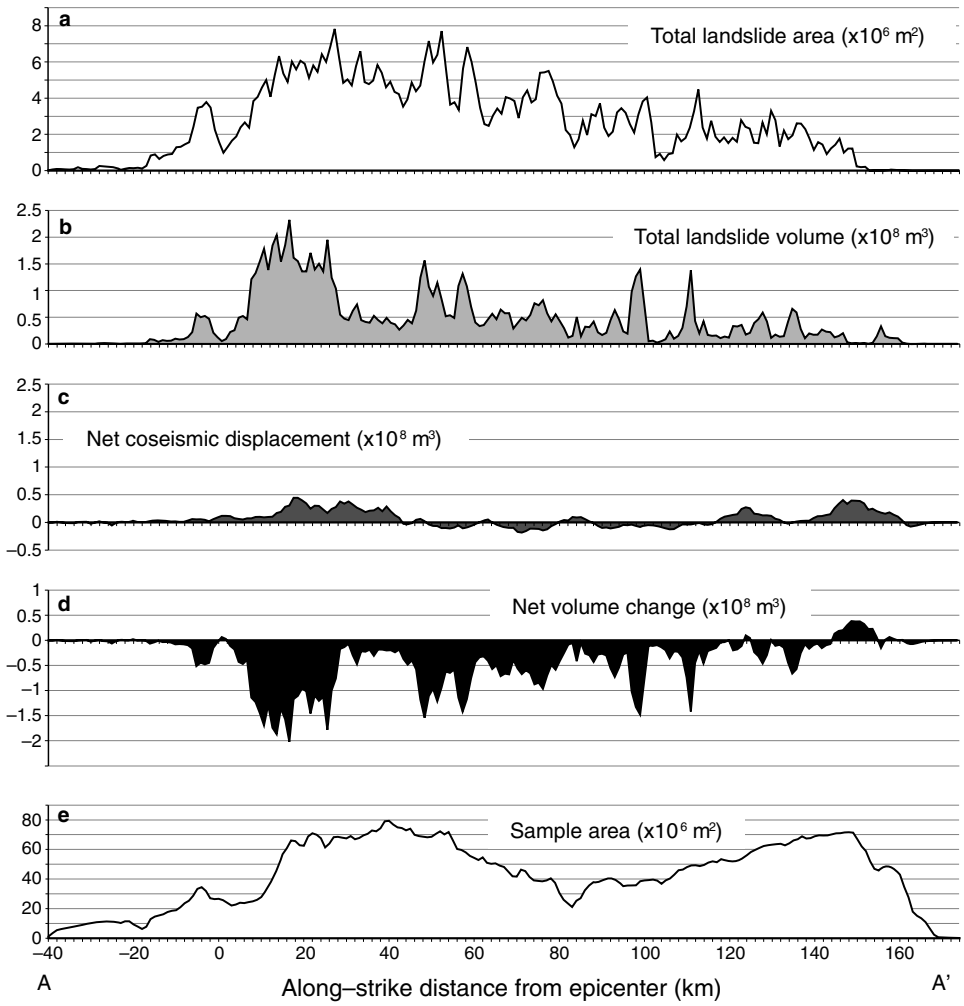


**Fig. 3.8.** Variations in landslide occurrence and coseismic displacement along the array of faults ruptured in the $M_w$ 7.9 2008 Wenchuan earthquake. All data are projected onto a rupture-parallel line at 1-km intervals. Distance along horizontal axis is given with respect to the perpendicular projection of the epicenter of the main shock onto the fault trend. (a) Total area of landslides within each 1-km-wide strip. (b) Landslide volume derived from a global bedrock landslide-scaling relationship applied to individual landslides within each 1-km-wide strip. (c) Net coseismic displacement (volume change) in each 1-km-wide strip. (d) Potential net volume change determined by subtracting landslide volumes from coseismic volume change. (e) Along-strike distribution of sample area covered by satellite imagery. Local minima in landslide area and volume are not correlated with small sample areas. (From Parker *et al.*, 2011.)

substrate properties, topography, and the propensity to failure of seismically excited locations. These patterns of erosion may persist after a seismic event, dissipating gradually as subsequent drivers mobilize weakened material and shift it through sediment routing systems. In addition, seismically triggered landsliding and subsequent induced erosion can significantly reduce – or even negate – the uplift caused by an earthquake.

These conclusions are derived from quantitative analysis of a small number of geophysically well-instrumented and geomorphologically well-documented cases. Broader underpinning for each of these conclusions will require detailed observations of other historic and future cases of landsliding due to dip–slip and strike–slip earthquakes, with special attention to their seismological dimensions and tectonic setting. The reward will be a deeper insight into the root causes of earthquake-induced landsliding that can be used for scientific gain and societal benefit. With this insight, it will be possible to explore the stochastic nature of seismically induced erosion, and sediment production and routing with topological and temporal precision, thus providing a better understanding of the variability of sediment fluxes from tectonically active landscapes. It will also be possible to introduce earthquakes into landscape evolution models in a way that covers both their constructive and destructive effects, which is likely to result in an improved ability to explain the topography of faulted terrains and will give impetus to the debate on the role of earthquakes in orogenesis. Further, it may increasingly become possible to invert geomorphological observations on landslide populations for the geophysical understanding of faulting and the mechanisms of shallow earthquakes. Finally, it will become possible to quantitatively constrain both site-specific and statistical evaluations of the risk of seismically triggered and induced landsliding, with due regard to the prolonged geomorphological effect of an instantaneous seismic event. These advances could result in a redefinition of natural disaster scenarios for the impact of earthquakes on landslide-prone landscapes and better-informed decisions about the repair and socio-economic regeneration of epicentral areas in steep uplands. Further advances will require

- better constraints on background rates and patterns of landsliding and post-seismic sediment transport
- rapid, comprehensive, and detailed observation of landslides in areas affected by earthquakes

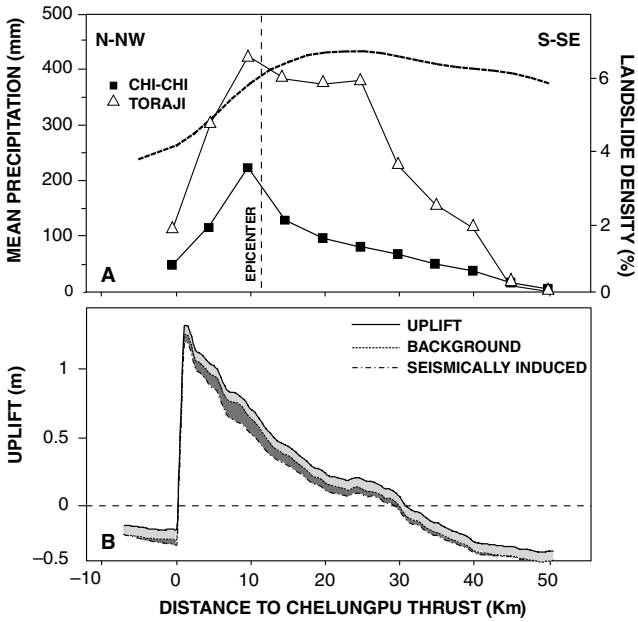


**Fig. 3.9.** Distribution of uplift and erosion caused by the 1999 Chi-Chi earthquake, Taiwan. (A) Density of landslides triggered by the earthquake and typhoon Toraji (2001), plotted against distance to the surface trace of the Chelungpu fault. The density distribution of typhoon-triggered landslides has the same general pattern as the coseismic landslides, but also reflects the spatial pattern of rainfall intensity shown by the bold black line. (B) Topographic effect of the Chi-Chi earthquake through the Choshui catchment. Seismic uplift of catchment surface (black line) has been reduced by background erosion (light gray), assumed to be uniformly distributed, and by additional erosion caused by the earthquake (dark gray), distributed according to density of coseismic landslides. (From Hovius *et al*., 2011.)

- instrumental measurements of ground motion in these areas
- a better understanding of geologic and topographic controls on landslide susceptibility
- improved knowledge of the causes of weakening of near-surface materials due to strong ground motion.

## REFERENCES


Abrahamson, N.A. and Somerville, P.G. (1996). Effects of the hanging wall and footwall on ground motions recorded during the Northridge earthquake. *Bulletin of the Seismological Society of America*, 86, 93–99.

Aki, K. (1993). Local site effects on weak and strong ground motion. *Tectonophysics*, 218, 93–111.

Allen, C.R., Brune, J.N., Cluff, L.S. and Barrows, A.G., Jr. (1998). Evidence for unusually strong near-field ground motion on the hanging wall of the San Fernando Fault during the 1971 earthquake. *Seismological Research Letters*, 69, 524–531.

Anderson, J.G. (2000). Expected shape of regressions for ground-motion parameters on rock. *Seismological Society of America Bulletin*, 90, 43–52.

Anderson, J.G., Brune, J.N., Anooshehpoor, A. and Ni, S.D. (2000). New ground motion data and concepts in seismic hazard analysis. *Current Science*, 79, 1278–1290.

Avouac, J.P. (2007). Dynamic processes in extensional and compressional settings: Mountain building – from earthquakes to geological deformation. In *Treatise on Geophysics*, ed. G. Schubert. Amsterdam: Elsevier, pp. 377–439.

Bindi, D., Luzi, L., Massa, M. and Pacor, F. (2010). Horizontal and vertical motion prediction equations derived from the Italian Accelerometric Archive (ITACA). *Bulletin of Earthquake Engineering*, 8, 1209–1230.

Boore, D.M. and Atkinson, G.M. (2008). Ground motion prediction equations for the average horizontal component of PGA, PGV, and 5%-damped PSA at spectral periods between 0.01 s and 10 s. *Earthquake Spectra*, 24, 99–138.

Bouchon, M. (1973). Effect of topography on surface motion. *Seismological Society of America Bulletin*, 63, 615–632.

Bouchon, M. and Baker, J. (1996). Seismic response of a hill: The example of Tarzana, California. *Seismological Society of America Bulletin*, 86, 66–72.

Bufe, G.C. and Perkins, D.M. (2005). Evidence for a global seismic-moment release sequence. *Seismological Society of America Bulletin*, 95, 833–853.

Burbank, D.W., Leland, J., Fielding, E. *et al.* (1996). Bedrock incision, rock uplift and threshold hillslopes in the northwestern Himalayas. *Nature*, 379, 505–510.

Chigira, M., Wu, X., Inokuchi, T. and Wang, G. (2010). Landslides induced by the 2008 Wenchuan earthquake, Sichuan, China. *Geomorphology*, 118, 225–238.

Chiou, B. and Youngs, R. (2008). An NGA model for the average horizontal component of peak ground motion and response spectra. *Earthquake Spectra*, 24, 173–215.

Dadson, S.J., Hovius, N., Chen, H. *et al.* (2004). Earthquake-triggered increase in sediment delivery from an active mountain belt. *Geology*, 32, 733–736.

Dai, F.C., Xu, C., Yao, X. *et al*. (2011). Spatial distribution of landslides triggered by the 2008 Ms 8.0 Wenchuan earthquake. *Journal of Asian Earth Sciences*, 40, 883–895.

de Michele, M., Raucoules, D., de Sigoyer, J., Pubellier, M. and Chamot-Rooke, N. (2010). Three-dimensional surface displacement of the 2008 May 12 Sichuan earthquake (China) derived from Synthetic Aperture Radar: Evidence for rupture on a blind thrust. *Geophysics Journal Internationa*l, 183, 1097–1103.

Del Gaudio, V. and Wasowski, J. (2007). Directivity of dynamic slope response to seismic shaking. *Geophysical Research Letters*, 34, doi:10.1029/2007GL029842.

Densmore, A.L. and Hovius, N. (2000). Topographic fingerprints of bedrock landslides. *Geology*, 28, 371–374.

Field, E.H., Johnson, P.A., Beresnev, I.A. and Zeng, Y. (1994). Nonlinear ground-motion amplification by sediments during the 1994 Northridge earthquake. *Nature*, 390, 599–602.

Geli, L., Bard, P.-Y. and Jullien, B. (1988). The effect of topography on earthquake ground motion: A review and new results. *Seismological Society of America Bulletin*, 78, 42–63.

Guzzetti, F., Ardizzone, F., Cardinali, M., Rossi, M. and Valigi, D. (2009). Landslide volumes and landslide mobilization rates in Umbria, central Italy. *Earth and Planetary Science Letters*, 279, 222–229.

Hanks, T.C. and Kanamori, H. (1979). Moment magnitude scale. *Journal of Geophysical Research*, 84, 2348–2350.

Harp, E.L. and Jibson, R.W. (1996). Landslides triggered by the 1994 Northridge, California earthquake. *Seismological Society of America Bulletin*, 86, 319–332.

Havenith, H.-B., Vanini, M., Jongmans, D. and Faccioli, E. (2003). Initiation of earthquake-induced slope failure: Influence of topographical and other site-specific amplification effects. *Journal of Seismology*, 7, 397–412.

Hikima, K. and Koketsu, K. (2005). Rupture processes of the 2004 Chuetsu (mid-Niigata prefecture) earthquake, Japan: A series of events in a complex fault system. *Geophysical Research Letters*, 32, L18303.

Honda, R., Aoi, S., Morikawa, N. *et al*. (2005). Ground motion and rupture process of the 2004 Mid Niigata Prefecture earthquake obtained from strong motion data of K-NET and KiK-net. *Earth, Planets and Space*, 57, 527–532.

Hovius, N., Stark, C. P. and Allen, P. A. (1997). Sediment flux from a mountain belt derived by landslide mapping. *Geology*, 25, 231–234.

Hovius, N., Meunier, P., Lin, C. W. *et al*. (2011). Prolonged seismically induced erosion and the mass balance of a large earthquake. *Earth and Planetary Science Letters*, 304, 347–355.

Hsu, Y. J., Avouac, J. P., Yu, S. B. *et al*. (2009). Spatio-temporal slip, and stress level on the faults within the western foothills of Taiwan: Implications for fault frictional properties. *Pure and Applied Geophysics*, 166, 1853–1884.

Hung, J. J. (2000). Chi-Chi earthquake induced landslides in Taiwan. *Earthquake Engineering and Engineering Seismology*, 2, 25–33.

Jacoby, G. C. (1997). Application of tree ring analysis to paleoseismology. *Reviews of Geophysics*, 35, 109–124.

Kao, H. and Chen, W. P. (2000). The Chi-Chi earthquake sequence: Active, out-of-sequence thrust faulting in Taiwan. *Science*, 288, 2346–2349.

Kawabata, D. and Bandidas, J. (2009). Landslide susceptibility mapping using geological data, a DEM from ASTER images and an Artificial Neural Network (ANN). *Geomorphology*, 113, 97–109.

Keefer, D. K. (1984). Landslides caused by earthquakes. *Geological Society of America Bulletin*, 95, 406–421.

(1994). The importance of earthquake-induced landslides to long-term slope erosion and slope-failure hazards in seismically active regions. *Geomorphology*, 10, 265–284.

(1999). Earthquake-induced landslides and their effects on alluvial fans. *Journal of Sedimentary Research*, 69, 84–104.

(2002). Investigating landslides caused by earthquakes: A historical review. *Surveys in Geophysics*, 23, 473–510.

Kelsey, H. M. (1988). Formation of inner gorges. *Catena*, 15, 433–458.

Koi, T., Hotta, N., Ishigaka, I. *et al*. (2008). Prolonged impact of earthquake-induced landslides on sediment yield in a mountain watershed: The Tanzawa region, Japan. *Geomorphology*, 101, 692–702.

Korup, O. (2005). Large landslides and their effect on alpine sediment flux: South Westland, New Zealand. *Earth Surface Processes and Landforms*, 30, 305–323.

Larsen, I. J., Montgomery, D. R. and Korup, O. (2010). Landslide erosion controlled by hillslope material. *Nature Geoscience*, 3, 247–251, doi:10.1038/ngeo776.

Lin, G. W., Chen, H., Hovius, N. *et al*. (2008). Effects of earthquake and cyclone sequencing on landsliding and fluvial sediment transfer in a mountain catchment. *Earth Surface Processes and Landforms*, 33, 1354–1373, doi:10.1002/esp1716.

Liu, Y. and Rubin, A. M. (2010). Role of fault gouge dilatancy on aseismic deformation transients. *Journal of Geophysical Research*, 115, B10414, doi:10.1029/2010JB007522.

Loevenbruck, A., Cattin, R., Le Pichon, X., Dominguez, S. and Michel, R. (2004). Coseismic slip resolution and post-seismic relaxation time of the 1999 Chi-Chi, Taiwan, earthquake as constrained by geological observations, geodetic measurements and seismicity. *Geophysical Journal International*, 158, 310–326.

Luzi, L. and Pergalani, F. (2000). A correlation between slope failures and accelerometric parameters: The 26 September 1997 earthquake (Umbria-Marche, Italy). *Soil Dynamics and Earthquake Engineering*, 20, 301–313.

Malamud, B. D., Turcotte, D. L., Guzzetti, F. and Reichenbach, P. (2004). Landslides, earthquakes, and erosion. *Earth and Planetary Science Letters*, 229, 45–59.

Mathur, L. P. (1953). Assam earthquake of 15th August 1950: A short note on factual observations. In *A Compilation of Papers on the Assam Earthquake of August 15, 1950*, ed. M. B. Ramachandra Rao. National Geographical Research Institute, Hyderabad, Central Board of Geophysics Publication 1, pp. 56–60.

Meisling, K. E. and Sieh, K. E. (1980). Disturbance of trees by the 1857 Fort Tejon earthquake, California. *Journal of Geophysical Research*, 85, 3225–3238.

Meunier, P., Hovius, N. and Haines, A. J. (2007). Regional patterns of earthquake-triggered landslides and their relation to ground motion. *Geophysical Research Letters*, 34, L20408, doi:10.1029/2007GL031337.

(2008). Topographic site effects and the location of earthquake-induced landslides. *Earth and Planetary Science Letters*, 275, 221–232.

Newmark, N. M. (1965). Effects of earthquakes on dams and embankments. *Geotechnique*, 15, 139–160.

Ogelsby, D. D., Archuleta, R. J. and Nielsen, S. B. (2000). The three-dimensional dynamics of dipping faults. *Seismological Society of America Bulletin*, 90, 616–628.

Oldham, R. D. (1899). *Report on the Great Earthquake of 12th June 1897*. Geological Survey of India, Memoir 29.

Osanai, N., Uchida, T., Noro, T. *et al.* (2007). Application of the empirical method of assessing the potential of slope failures to Niigata–ken Chuetsu Earthquake. *Journal of the Japanese Society of Erosion Control Engineering*, 59, 60–65.

Owen, L. A., Kamp, U., Khattak, G. A. *et al*. (2008). Landslides triggered by the 8 October 2005 Kashmir earthquake. *Geomorphology*, 94, 1–9.

Pain, C. F. and Bowler, J. M. (1973). Denudation following the 1970 earthquake at Madang, Papua New Guinea. *Zeitscrift für Geomorphologie*, 18, 92–104.

Parise, M. and Jibson, R. W. (2000). A seismic landslide susceptibility rating of geologic units based on analysis of characteristics of landslides triggered by the 17 January, 1994 Northridge, California earthquake. *Engineering Geology*, 58, 251–270.

Parker, R. N., Densmore, A. L., Rosser, N. J. *et al.* (2011). Mass wasting triggered by the 2008 Wenchuan earthquake exceeds orogenic growth. *Nature Geoscience*, 4, doi:10.1038/ngeo1154.

Pearce, A. and O'Loughlin, C. L. (1985). Landsliding during a M7.7 earthquake: Influence of geology and topography. *Geology*, 13, 855–858.

Pearce, A. J. and Watson, A. J. (1986). Effects of earthquake-induced landslides on sediment budget and transport over 50 years. *Geology*, 14, 52–55.

Rodriguez, C. E., Bommer, J. J. and Chandler, R. J. (1999). Earthquake-induced landslides; 1980–1997. *Soil Dynamics and Earthquake Engineering*, 18, 325–346.

Schmedes, J. and Archuleta, R. J. (2008). Near-source ground motion along strike-slip faults: Insights into magnitude saturation of PGV and PGA. *Seismological Society of America Bulletin*, 98, 2278–2290.

Shen, Z. K., Sun, J., Zhang, P. *et al*. (2009). Slip maxima at fault junctions and rupturing of barriers during the 2008 Wenchuan earthquake. *Nature Geoscience*, 2, 718–724.

Shi, B., Anooshehpoor, A., Brune, J. N. and Zeng, Y. (1998). Dynamics of thrust faulting: 2-D lattice model. *Seismological Society of America Bulletin*, 88, 1484–1494.

Shin, T. C. and Teng, T. L. (2001). An overview of the 1999 Chi-Chi, Taiwan, earthquake. *Seismological Society of America Bulletin*, 91, 895–913.

Simonett, D. S. (1967). Landslide distribution and earthquakes in the Bewani and Torricelli Mountains, New Guinea: A statistical analysis. In *Landform Studies from Australia and New Guinea*, ed. J. N. Jennings and J. A. Mabbutt. Cambridge, UK: Cambridge University Press, pp. 64–84.

Sommerville, P. G., Smith, N., Graves, R. and Abrahamson, N. (1997). Modification of empirical strong ground motion attenuation relations for the amplitude and duration effects of rupture directivity. *Seismological Research Letters*, 68, 199–222.

Sommerville, P. G., Irikura, K., Graves, R. *et al.* (1999). Characterizing earthquake slip models for the prediction of strong ground motion. *Seismological Research Letters*, 70, 59–80.

Spudich, P. (ed.). (1996). *The Loma Prieta, California Earthquake of October 17, 1989: Main Shock Characteristics*. US Geological Survey, Professional Paper 1550-A.

Spudich, P., Hellweg, M. and Lee, W. H. K. (1996). Directional topographic site response at Tarzana observed in aftershocks of the 1994 Northridge, California, earthquake: Implications for mainshock motions. *Seismological Society of America Bulletin*, 86, 193–208.

Suzuki, W., Aoi, S. and Sekigushi, H. (2010). Rupture process of the 2008 Iwate–Miyagi Nairiku, Japan, earthquake derived from near-source strong-motion records. *Geological Society of America Bulletin*, 100, 256–266.

Taylor, S. R., Bonner, B. P. and Zandt, G. (1986). Attenuation and scattering of broadband P and S waves across North America. *Journal of Geophysical Research*, 91, 7309–7325.

Todorovska, M. I. and Trifunac, M. D. (1997). Amplitudes, polarity and time of peaks of strong ground motion during the 1994 Northridge, California, earthquake. *Soil Dynamics and Earthquake Engineering*, 16, 235–258.

Trifunac, M. D. (1994). Q and high frequency strong ground motion spectra. *Soil Dynamics and Earthquake Engineering*, 13, 149–161.

Wang, C. Y., Cheng, L. H., Chin, C. V. and Yu, S. B. (2001). Coseismic hydrologic response of an alluvial fan to the 1999 Chi-Chi earthquake, Taiwan. *Geology*, 29, 831–834.

Wang, H. B., Sassa, K. and Xu, W. Y. (2007). Analysis of a spatial distribution of landslides triggered by the 2004 Chuetsu earthquakes of Niigata Prefecture, Japan. *Natural Hazards*, 41, 43–60.

Wells, D. L. and Coppersmith, K. J. (1994). Analysis of empirical relationships among magnitude, rupture length, rupture area, and surface displacement. *Seismological Society of America Bulletin*, 84, 974–1002.

Wilson, R. C. and Keefer, D. K. (1979). Dynamic analysis of slope failure from the 6 August 1979 Coyote Lake, California, earthquake. *Seismological Society of America Bulletin*, 73, 863–877.

Yagi, H., Sato, G., Hikagi, D., Yamamoto, M. and Yamasaki, T. (2009). Distribution and characteristics of landslides induced by the Iwate–Miyagi Nairiku earthquake in 2008 in Tohoku District, Northeast Japan. *Landslides*, 6, 335–344.

Yanites, B. J., Tucker, G. E., Mueller, K. J. and Chen, Y. G. (2010). How rivers react to large earthquakes: Evidence from central Taiwan. *Geology*, 38, 639–642.

Yin, J., Chen, J., Xu, X.-W., Wang, X. and Zheng, Y. (2010). The characteristics of the landslides triggered by the Wenchuan $M_s$ 8.0 earthquake from Anxian to Beichuan. *Journal of Asian Earth Sciences*, 37, 452–459.

Yu, S. B., Kuo, L. C., Hsu, Y. J. *et al.* (2001). Preseismic deformation and coseismic displacements associated with the 1999 Chi-Chi, Taiwan, earthquake. *Seismological Society of America Bulletin*, 91, 995–1012.